Modern Band Theory of Disordered Alloys: Basic Concepts Including a Discussion of Momentum Densities *

A. Bansil

Department of Physics, Northeastern University, Boston, MA 02115

Z. Naturforsch. **48a**, 165–179 (1993); received January 25, 1992

An overview of some of the basic concepts in the modern first-principles band theory of disordered alloys is given. The question of how the notion of Bloch energy bands and Fermi surfaces generalizes to the case of the disordered system, insofar as the *average* electronic spectrum is concerned, is stressed. The theory is illustrated with examples chosen from the work on binary alloys; a few examples of the very recent studies of disordered phases of the high-T_c superconductors are also included. The application of the alloy theory to obtain electron and electron-positron momentum densities involved in the analysis of Compton scattering and positron annihilation (angular correlation) experiments in alloys is discussed, with a selection of relevant theoretical and experimental studies.

Key words: Disordered alloys; KKR-CPA; Momentum densities; Compton scattering; Positron annihilation (ACAR).

I. Introduction

By the early 1970s, it was evident from the extensive work on tight-binding Hamiltonians that the coherent potential approximation (CPA) provides a reasonable mean-field theory of the average electronic properties of random substitutional alloys. These simple model Hamiltonians, however, are not adequate for discussing the electronic spectra of alloys in any detail. There was thus a natural impetus to consider the application of the CPA to the muffin-tin Hamiltonian, which is well-known to provide a realistic description of the crystal potential in close-packed systems, especially in metals; by inserting suitably placed "empty" spheres to increase the packing fraction, a reasonable treatment of more open structures is also possible. This effort has led to the development of a successful first-principles band theory of disordered alloys. The formalism, which makes extensive use of the multiple scattering approach and is thus limited to neither the strong nor the weak scattering regimes, reduces to the Korringa-Kohn-Rostoker (KKR) band structure scheme in the perfect-crystal limit and for this reason is usually referred to as the KKR-CPA [1–7].

It is noteworthy that the Bloch energy band theory for a perfect crystal hinges on the presence of long-range order in the system. Therefore, this theory cannot be applied directly to the case of a disordered alloy where the translational symmetry is broken. Nevertheless, insofar as the *average* properties of the alloy are concerned, substantial progress is possible by replacing the disordered system by an *ordered* one of suitably chosen effective atoms. It is this class of approximations, the so-called single-site approximations, to which the CPA belongs. The periodicity thus having been restored, the notions of energy bands, Fermi surfaces, Brillouin zones, etc., then occur naturally in describing the alloy spectrum, *albeit* with certain inherent subtleties. There is clear experimental evidence that, despite the lack of long-range order, these concepts continue to play a useful role in wide classes of disordered alloys.

The purpose of this article is twofold. First, we discuss some of the basic concepts underlying the modern band theory of disordered alloys. Second, we provide an overview of the application of the KKR-CPA-type approach to obtain electron and electron–positron momentum densities relevant for an analysis of the Compton scattering and the angular correlation of positron annihilation radiation (ACAR) experiments. Within the limitations of space, many topics are hardly mentioned or not touched at all. Among these are recent important advances in formalism and application to multi-atom-per-unit-cell complex struc-

* Presented at the Sagamore X Conference on Charge, Spin and Momentum Densities, Konstanz, Fed. Rep. of Germany, September 1–7, 1991.

Reprint requests to Prof. A. Bansil, Department of Physics, Northeastern University, Boston, MA 02115, USA.

0932-0784 / 93 / 0100-0165 $ 01.30/0. – Please order a reprint rather than making your own copy.

tures, extensions of the theory to treat ordering and clustering effects, relativistic effects, attempts to go beyond the single-site-approximation CPA framework, and efforts to include non-muffin-tin corrections to the muffin-tin Hamiltonian. Many physical properties of alloys have been investigated within the KKR-CPA framework, including momentum densities, charge densities, band spectroscopies, itinerant magnetism, phase stabilities, transport, and a variety of related issues. The set of review articles and references cited should, however, allow the interested reader access to the relevant literature [1–25].

An outline of this article is as follows. The introductory remarks are followed in Sect. II by an overview of the alloy theory, including brief comments on the common single-site approximations, namely, the virtual crystal (VCA), the average t-matrix (ATA), and the coherent potential (CPA) approximations. We discuss how the concept of the Bloch energy bands and the Fermi surface generalizes to the disordered case, with illustrative examples drawn from mostly the binary alloys. As examples of complex systems, a few results pertaining to the very recent work on the high-T_c superconductors, namely, the simple cubic perovskites [11], $Ba_xK_{1-x}BiO_3$ and $BaPb_{1-x}Bi_xO_3$, and the body-centered tetragonal $La_{1-x}Sr_xCuO_4$, are presented [7]. Section III turns to the question of electron and electron–positron momentum densities [18–25]. Here, brief remarks on the relevant KKR-CPA formalism are followed by illustrative results in a number of Cu-based alloys, which have been the subject of numerous theoretical and experimental studies. Section IV makes some concluding remarks.

II. An Overview of the Alloy Theory

a) Formalism

We are concerned with the average electronic spectrum (i.e., an average over the possible microscopic configurations of the constituent atoms) of the random substitutionally disordered alloy A_xB_{1-x}. The fundamental idea behind the alloy band theory is to replace the disordered system by an *ordered* system of appropriately chosen effective atoms, as represented by Figure 1.

To proceed further, the effective atom needs to be specified. This introduces other well-defined approximations [1–7]. The simplest is the virtual-crystal approximation (VCA), where the effective potential,

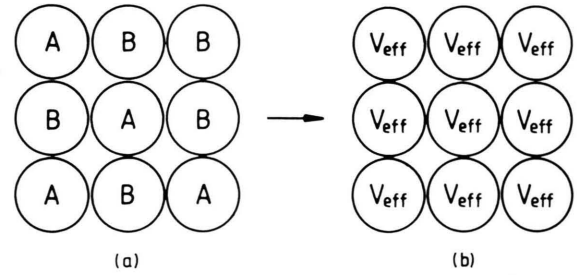

Fig. 1. A schematic illustration of how the disordered assembly of A and B atoms is replaced by an ordered crystal of effective atoms for discussing the average properties of the alloy.

V_{VCA}, is the average of the A and B potentials:

$$V_{VCA} = x\,V_A + (1-x)\,V_B\,. \tag{1}$$

VCA is generally a poor scheme for describing systems that are strongly disordered in the sense that V_A and V_B differ substantially. Also, in view of (1), V_{VCA} is a real quantity, so that the VCA yields a strictly vanishing disorder smearing of states.

In the average-t-matrix approximation (ATA), one averages the A and B atom t-matrices, rather than the potentials, i.e.

$$t^{ATA} = x\,t^A + (1-x)\,t^B\,. \tag{2}$$

The t-matrix is related straightforwardly to the atomic potential V by the equations of potential scattering. Despite its relative simplicity, the ATA has been found to capture the dominant physics of disorder in wide classes of alloys.

Finally, the coherent potential approximation (CPA) is specified by the condition that the average scattering from A and B atoms placed in the CPA medium vanishes, i.e.,

$$x\,t_A^{eff} + (1-x)\,t_B^{eff} = 0\,. \tag{3}$$

Here, t_A^{eff} and t_B^{eff} respectively denote the t-matrices of A and B atoms placed in the effective medium. Equation (3) is to be solved for the unknown quantity t^{eff}, the solution being $t^{eff} \equiv t^{CPA}$.

The modern alloy theory is based on the application of the single-site approximation to treat disorder effects within the framework of the muffin-tin Hamiltonian. The CPA is the most satisfactory of the approximations as it treats disorder selfconsistently. The resulting KKR-CPA formalism proceeds naturally in terms of the angular-momentum representation, making extensive use of the multiple scattering theory

techniques. The central objects in the formalism are the ensemble-averaged one-particle Green's function $G(z)$, whose imaginary part is related to the average density of states, and the one-site restricted averages of the Green's function, $G_A(z)$ and $G_B(z)$, which yield the effective charge densities in the A and B spheres. Most recently, [10] has rigorously extended the KKR-CPA Green's function into the complex energy plane and exploited its analytic properties to obtain a powerful scheme for a parameter-free charge- and spin-selfconsistent treatment of the electronic structure of complex multi-component alloys with many atoms per unit cell; furthermore, by invoking the spectral representation of the Green's function, we are able to apply a tetrahedron-type $\boldsymbol{k}$-space integration method in the theory of muffin-tin alloys, permitting us to treat for the first time the ordered compounds, the single-impurity problem, and the concentrated disordered alloys with the same set of computer codes. We refer to [10] and various review articles for a discussion of these and related aspects of the KKR-CPA methodology and formalism [1–7, 9, 12].

b) Complex Energy Bands

The concept of a Bloch energy level perhaps plays the most fundamental role in the band theory of perfect crystals. It turns out that something similar can still be defined in a disordered alloy, even though the system does not possess long-range order. As in the case of a perfect crystal, the "energy bands" for the ordered medium of effective atoms can be shown to be given by the secular equation [1, 2]

$$\| t_{\text{eff}}^{-1}(E) - B(\boldsymbol{k}, E) \| = 0 . \tag{4}$$

Here, the determinant is implicitly taken to be in the angular-momentum space (i.e. the space of orbital and magnetic quantum numbers, $L \equiv (l, m)$). The $B(\boldsymbol{k}, E)$ matrix depends only on the crystal lattice and is independent of the atomic potentials. In a perfect A (or B) crystal, $t_{\text{eff}} \to t_A$ (or t_B) and (4) reduces to the KKR equation used widely to compute energy bands in perfect crystals. Equation (4) therefore forms a natural basis for constructing a band theory of random alloys. If we fix the value of the crystal momentum $\boldsymbol{k}$ and solve (4) for the bands $E(\boldsymbol{k})$, the solutions are real in a perfect crystal, but become complex numbers in the alloy. The presence of a non-zero imaginary part of energy levels is a fundamental physical effect which represents the disorder-induced smearing of states in an alloy.

Figure 2 shows typical complex energy bands in Cu-based alloys [26–29]. As indicated in the caption, some of the results are based on the ATA, while others on the CPA. The Cu-potential in Fig. 2a is also used in the $Cu_{90}Al_{10}$ and $Cu_{90}Ge_{10}$ computations. The $Cu_{70}Ni_{30}$ and $Cu_{70}Zn_{30}$ results use a different Cu-potential; nevertheless, all alloys are comparable insofar as the Cu d-band position is concerned. Whereas the various panels of Fig. 2 cannot be compared with each other in detail, this figure allows us to delineate similarities and differences in this series of alloys. In all cases, the Cu d-band complex is seen to suffer relatively small shifts on alloying. Ni induces new Ni-related d-bands (around 8.2 eV in Fig. 2b), which are heavily smeared due to disorder. The states of s-p symmetry (e.g. Γ_1, $X_{4'}$), on the other hand, are virtually unaffected by disorder in **Cu**Ni and are undamped. In contrast to Ni, the addition of Ge or Al causes large smearings and shifts in the s-p-type states, Figs. 2d and 2e. Among the polyvalent solutes, Zn gives rise to a narrow 3d-band (around -1.4 eV in Fig. 2c), whereas in **Cu**Ge, the impurity band is of s-p symmetry and is several electron-volt wide. It is clear that different impurities influence the spectrum of Cu in fundamentally different ways, and that the effective disorder parameter in transition and noble metal alloys possesses a very complicated nature. In general, the effective disorder parameter is $\boldsymbol{k}$-dependent and, even for a given $\boldsymbol{k}$-value, the disorder seen by states of various symmetries can differ qualitatively. Note that aspects of the alloy bands could be modelled within simpler schemes. For example, the growth of the Fermi surface of Cu with the addition of Zn is well described by the virtual-crystal approximation and also by the rigid-band model (RBM); in RBM, **Cu**Zn is assumed to possess the band structure of Cu, independent of Zn concentration, but the RBM fails completely in the energy range of the Zn 3d-resonance. The present band theory, however, encompasses various behaviors within a single framework.

The complex energy bands are amenable to direct experimental observation via angle-resolved photoemission (ARPES) measurements from surfaces of alloy single crystals. Many such studies have been carried out [16, 30–32]. Figure 3 presents an example of the uppermost valence bands in Cu, **Cu**Al, and **Cu**Ge solid solutions and indicates a good accord between theory and experiment. The disorder smearings of the complex bands, as deduced from the measured increase in spectral widths in these alloys, are

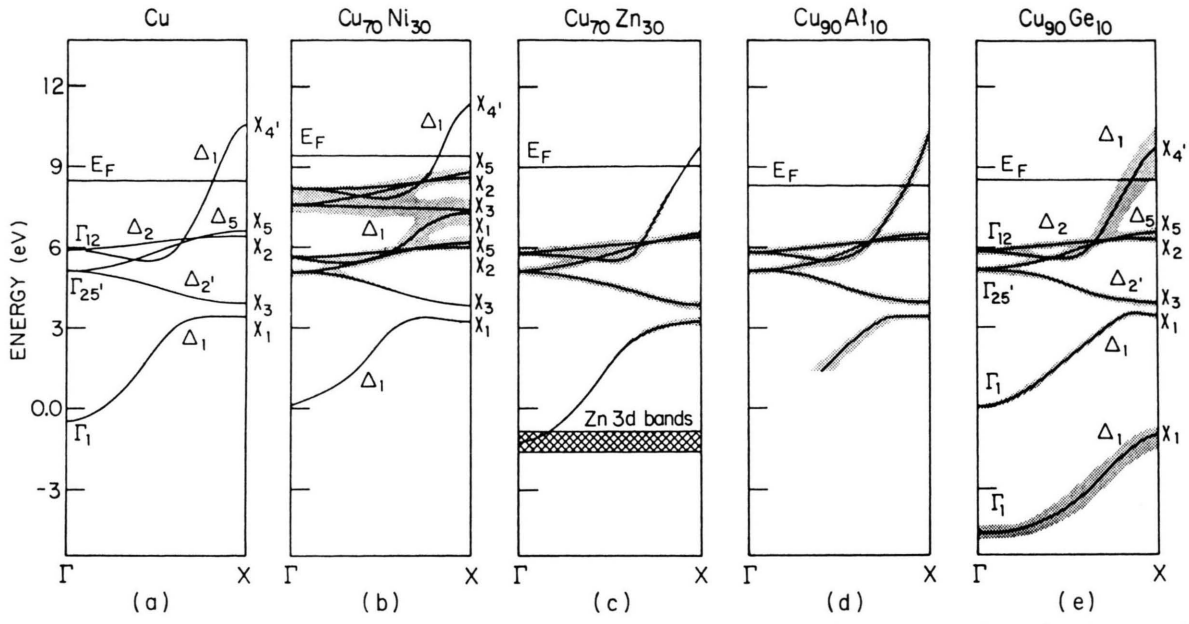

Fig. 2. Complex energy bands along the symmetry direction Γ–X in the Brillouin zone for (a): Cu, (b): $Cu_{70}Ni_{30}$ (ATA, Bansil et al. [26]), (c): $Cu_{70}Zn_{30}$ (ATA, Bansil et al. [27]), (d): $Cu_{90}Al_{10}$ (CPA, Asonen et al. [28]), and (e): $Cu_{90}Ge_{10}$ (CPA, Prasad and Bansil [29]). The vertical length of shading around the levels equals two times the imaginary part, Im $E(\boldsymbol{k})$, of the complex energies.

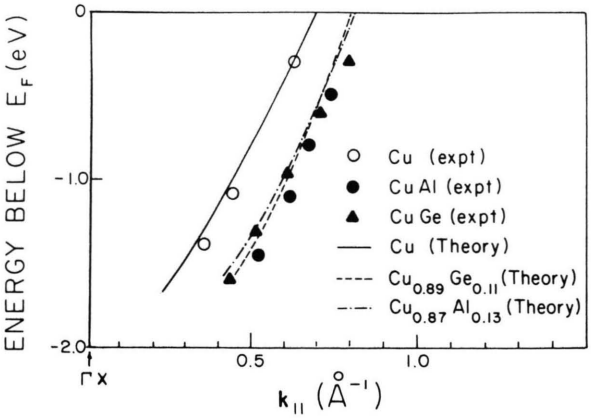

Fig. 3. Theoretical and experimental dispersion of the uppermost conduction band in Cu, **Cu**Al, and **Cu**Ge in the (100) mirror plane. $k_{\|}$ denotes the component of crystal momentum parallel to the (100) face. The imaginary parts of the alloy complex bands are not shown (after [31]).

also in reasonable accord with the corresponding theoretical predictions [31]. Figure 4 gives an example of a relativistic KKR-CPA computation compared with the ARPES experiments (a $Cu_{75}Pt_{25}$ (100)-surface is considered), showing once again a reasonable agreement between theory and experiment [13, 32].

In a perfect crystal, every Bloch level possesses a unit spectral weight. In sharp contrast, the complex energy levels do not possess uniform weights. For this reason, the average alloy density-of-states cannot be obtained by constructing a histogram of the complex energy levels. This difference between the complex bands and their perfect-crystal counterparts is a fundamental one and underlines the fact that a calculation of the density of states in the disordered system entails a level of intricacy well beyond the perfect crystal case.

It is noteworthy that, in a formal sense, the elementary quantity with a well-defined meaning in the formalism is the spectral density function $A_B(\boldsymbol{k}, E)$. In a perfect crystal, $A_B(\boldsymbol{k}, E)$ consists of a superposition of δ-functions at the Bloch levels $E(\boldsymbol{k})$. In the alloy, these δ-functions spread out into finite peaks. As illustrated by Fig. 5, the real and imaginary parts of the complex levels respectively yield the positions and half-widths of the associated peaks in $A_B(\boldsymbol{k}, E)$. In principle, the information given by the complex bands is thus contained in the plots of $A_B(\boldsymbol{k}, E)$ for various $\boldsymbol{k}$-values. However, the complex bands permit a convenient visualization and interpretation of the alloy spectrum.

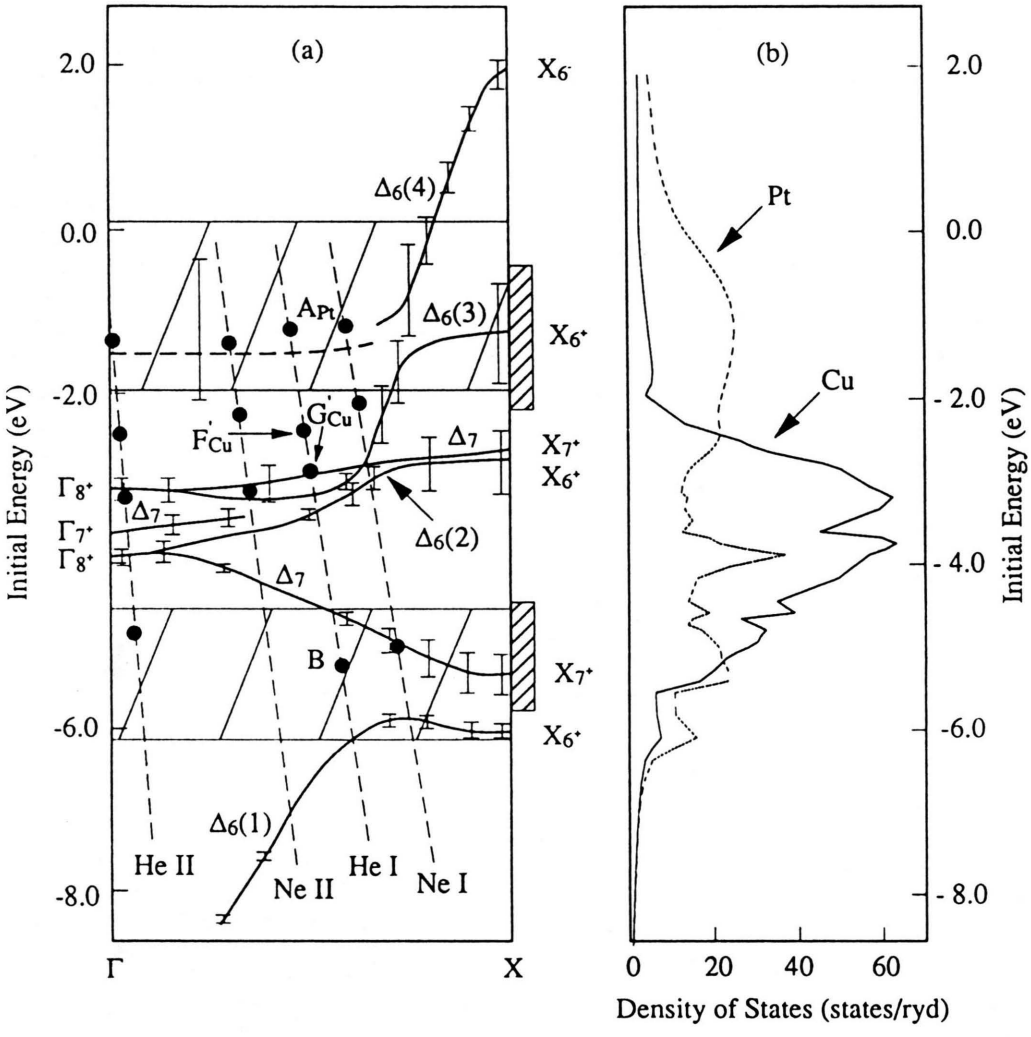

Fig. 4. (a) Relativistic KKR-CPA complex-energy bands in $Cu_{75}Pt_{25}$ along the symmetry direction Γ–X. Typical disorder-induced smearings of energy bands are represented by vertical bars around bands. Filled circles give the E, $\boldsymbol{k}$ points obtained from the angle-resolved photoemission measurements; dashed lines connecting these circles depict the final state (free electron) band shifted down on the energy scale by the corresponding photon energies. The hatched regions on the right-hand side of the panel give the average location and the FWHM of the Pt-derived structures in the ARPES spectra. (b) Cu (solid line) and Pt (dashed line) component densities of states in $Cu_{75}Pt_{25}$ (after [32]).

c) Alloy Fermi Surface

Many experiments show that the concept of the Fermi surface (FS) often continues to be useful in disordered alloys [2, 18–25, 15–17, 33]. As in the case of perfect crystals, the dimension of the alloy FS in a given direction in the Brillouin zone may be determined by the intersection of the Fermi energy E_F with the associated complex energy band. The smearing of states then implies that the alloy FS will not be sharply defined and that any point $\boldsymbol{k}(E_F)$ on the FS will possess a half-width $\Delta\boldsymbol{k}(E_F)$. Although $\Delta\boldsymbol{k}(E_F)$ and the imaginary part Im $E(\boldsymbol{k})$ of the complex levels represent the same physical effect, namely, the disorder induced smearing, the manner in which these two quantities occur in the theory should be distinguished. $|\Delta\boldsymbol{k}(E_F)|$ is the half-width of a peak in the spectral density, $A_B(\boldsymbol{k}, E_F)$, plotted as a function of $|\boldsymbol{k}|$ (in any

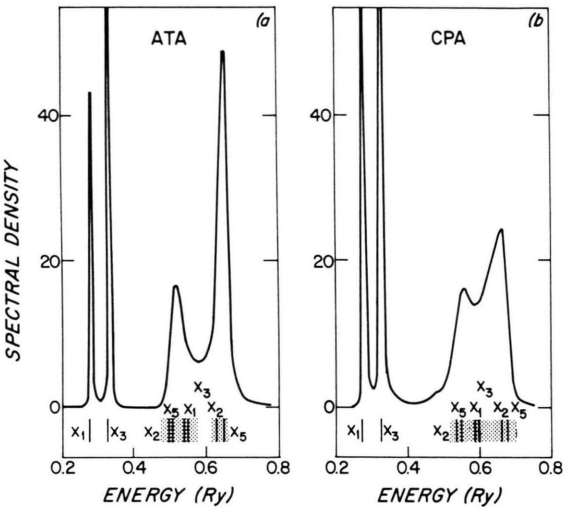

Fig. 5. ATA and CPA spectral density $A_B(\boldsymbol{k}, E)$ in $Cu_{75}Ni_{25}$ at the point X in the Brillouin zone. The complex levels at X are marked along the energy axis.

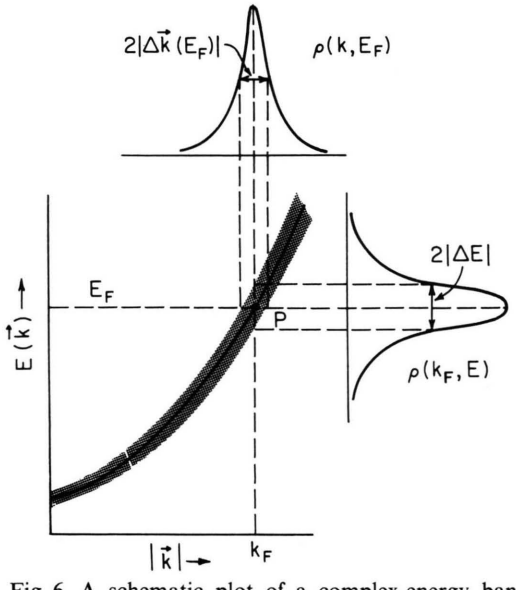

Fig. 6. A schematic plot of a complex-energy band. The meaning of the $\boldsymbol{k}$-width $2\,|\Delta\boldsymbol{k}(E_F)|$ and the associated E-width, $2\,|\Delta E|$ in terms of the spectral function $\varrho(\boldsymbol{k}, E)$ is illustrated.

direction), whereas Im $E(\boldsymbol{k})$ yields the half-width in energy, $|\Delta E|$, when $A_B(\boldsymbol{k}, E)$ is considered as a function of E for a fixed $\boldsymbol{k}$, see Figure 6.

Many studies of Fermi surfaces of concentrated alloys via positron annihilation (2D-ACAR) [18–25], and of dilute alloys via the de Haas-van Alphen effect (dHvA) [33] have been reported; some FS work via angle-resolved photoemission [16] in alloys also exists. We present a few illustrative examples now. Figure 7 shows that the shape of the FS in Cu and $Cu_{70}Zn_{30}$ is similar and that the theory and experiment are in good accord in this regard [34, 35]. The Fermi surfaces of noble-metal-based solid solutions are in fact expected to be similar, because the Fermi energy in these alloys often intersects only the uppermost valence band, which approximately preserves its shape on alloying, see Figure 2. The FS smearing in Fig. 7 is indicated by shading of the CPA curves. The length of the shading on any straight line drawn in the plane of the figure is 4 times the apparent half-width $\Delta\boldsymbol{k}(E_F)$ of the FS along this direction; for example, the half-width along the line B passing through the point P in Fig. 7b is nearly 3 to 4 times larger than along the line A.

The FS of **Cu**Ge presents an interesting case study [29], showing non-linear composition dependence of the radii, Figure 8. In the limit of low Ge concentration (≤ 0.5 at.% Ge), the neck as well as the belly radii increase at roughly half the rigid-band rate for quadrivalent impurities, in accord with the dHvA measurements [36, 37]. By contrast, in the high concentration regime (≥ 5 at.% Ge), the rate of change of the various FS radii corresponds to an effective Ge valence of somewhat less than 4. More recently, [38] reports a high-resolution 2D-ACAR investigation of the **Cu**Ge alloys, finding a good accord with KKR-CPA predictions of both the FS radii and their disorder-induced widths.

The non-linearity in the composition dependence of the FS of **Cu**Ge is related to the appearance of the Ge-derived impurity band well below the Fermi energy, see Figure 2e. Another striking instance of a system where changes deep within the spectrum influence the behavior of the FS is provided by α-PdH_x solid solutions. In this case, computations as well as dHvA measurements show that the FS changes non-uniformly on H uptake [39]; the Γ-centered electron sheets of Pd grow at approximately the rigid-band rate, while the hole pockets centered around X- and L-symmetry points shrink at only half the rigid-band rate. Also, the disorder smearing of the electron sheets in PdH_x is quite substantial, even though the states associated with the hole ellipsoids are virtually undamped.

Figure 9 considers FS radii in **Cu**Pd alloys. In this connection [40] focuses on the question of possible flattening of the FS of Cu along the [110] direction

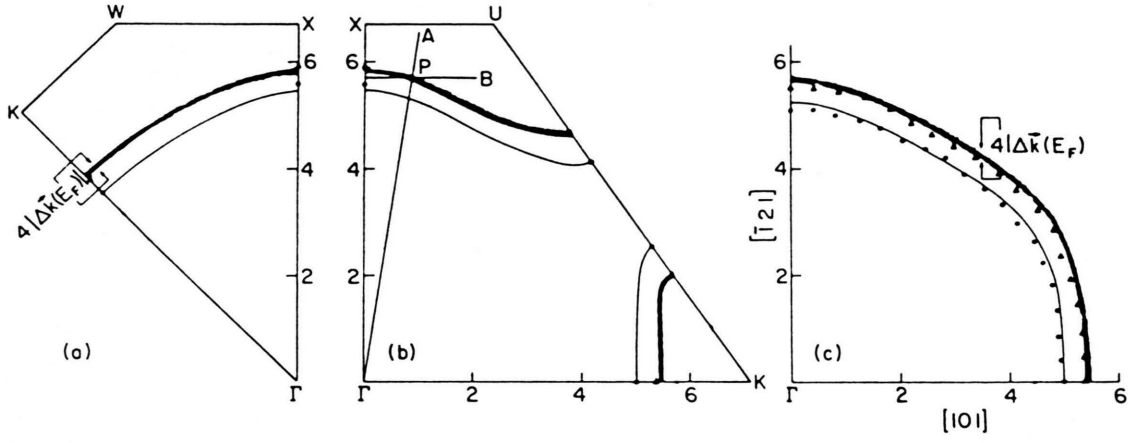

Fig. 7. Intersections of the Fermi surface of Cu (unshaded solid) and $Cu_{70}Zn_{30}$ (shaded) in three different planes in the Brillouin zone. Experimental points in Cu (circles) and $Cu_{70}Zn_{30}$ (triangles) are after [35]. The lines A and B in (b) are discussed in the text (after [34]).

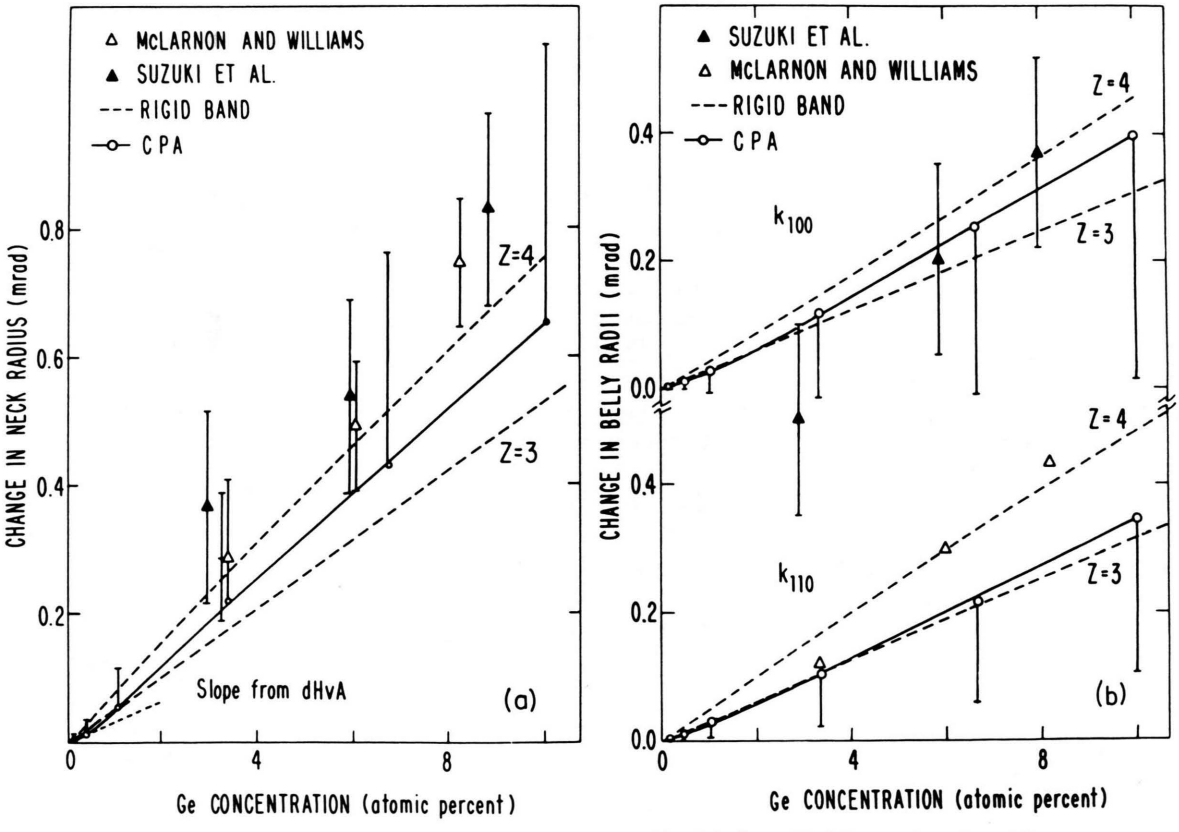

Fig. 8. The CPA changes in (a): the neck radius, and (b): the (100) and (110) belly radii of Cu as a function of Ge concentration. The disorder smearing $|\Delta \boldsymbol{k}(E_F)|$ is shown by vertical bars attached to the theoretical points. The dashed lines give the rigid-band results for solutes of valence $Z=3$ and $Z=4$. The experimental points [36] are indicated in the legend; the dHvA slope in (a) is from [37] (after [29]).

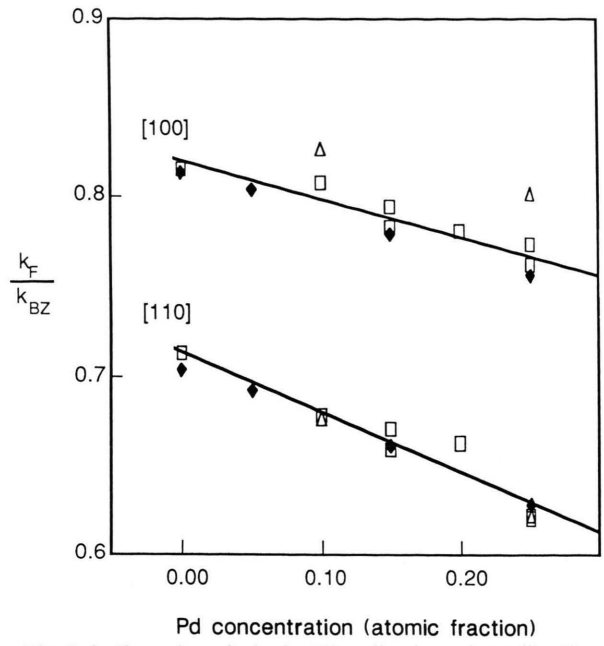

Fig. 9. k_F/k_{BZ} where k_F is the FS radius in a given direction and k_{BZ} is the Brillouin-zone dimension in the same direction. Radii along the [100] and [110] direction are shown. Least-squares fits through the data of [40] (open squares) are shown by solid lines. Theoretical results are: [42] (filled diamonds), and [41] (open triangles).

upon adding Pd. KKR-CPA calculations predict an appreciable flattening effect up to about 40 at.% Pd [41, 42]; the FS smearing in **Cu**Pd is rather small. This flattening is believed to be responsible for driving the short-range order that has been observed in CuPd alloys in diffuse electron and x-ray scattering studies [41]. The agreement between theory and experiment is good, especially with the KKR-CPA computations of [42]. The more rapid decrease of k_F/k_{BZ} in the [110] direction compared to the [100] direction provides clear evidence that the FS of Cu indeed flattens along [110] upon alloying. We note that such a flattening is seen in KKR-CPA calculations in other Cu-based alloys with decreasing electron/atom ratio as well as in rigid-band computations [34].

d) High-T_c Superconductor Alloys

We consider here some applications of the KKR-CPA scheme to complicated structures involving many atoms per unit cell, the examples so far having been limited to binary alloys.

The total KKR-CPA density of states in the simple cubic perovskites $Ba_xK_{1-x}BiO_3$ (BKB) and the $BaPb_{1-x}Bi_xO_3$ (BPB) is presented in Fig. 10 over the entire composition range [11]. The computations are charge self-consistent and involve no parameters other than the lattice data. Figure 11 compares the density of states at the Fermi energy (E_F) in the alloys with the corresponding predictions of the rigid band model based on the $BaBiO_3$ density of states. Figures 10 and 11 allow us to delineate the rigid band as well as non-rigid band changes in the spectrum of $BaBiO_3$ induced by (Ba-K) and (Bi-Pb) substitution.

Figure 10a shows that for energies around the Fermi energy of $BaBiO_3$, the shape of the density-of-states curve is little affected by Ba-K substitution. In contrast, the Pb-Bi substitution rapidly smooths the cusp at ≈ 0.6 Ry. This effect is related to the fact that the density of states around E_F in $BaBiO_3$ arises mainly from Bi- and O-sites, which are not influenced substantially when Ba is replaced by K; the Pb- and Bi-site densities, on the other hand, are quite different in this energy region and thus lead to considerable changes upon alloying. Interestingly though, the total density of states at E_F in both alloys (Fig. 11) is rather close to the predictions of a $BaBiO_3$-based rigid-band model [43, 44]. However, in view of the preceding observations, the agreement between the rigid-band and the KKR-CPA results in Fig. 11 in the case of BPB should be considered fortuitous rather than of an intrinsic significance.

Turning to the energy region of 0.15 to 0.45 Ry, Fig. 10 shows that the shape of the density-of-states curve is quite similar in BKB as well as BPB for $0.3 \leq E \leq 0.45$ Ry in the upper part of the Bi 6s–O 2p complex. For lower energies, $0.15 \leq E \leq 0.3$ Ry, we see substantial changes in the spectrum. For example, the largest peak at 0.29 Ry in $BaBiO_3$ splits and becomes less prominent in BKB; in contrast, this peak is rather unaffected in BPB. The relative weights, positions, and shapes of the density-of-states peaks at 0.23 Ry and 0.25 Ry in $BaBiO_3$ are influenced considerably in both BKB and BPB. The preceding changes in the spectra between 0.15 and 0.3 Ry arise not only from changes in the component densities of states associated with the substituted sites, but also from the indirect changes induced on the O- and other sites as a result of alloying.

Figure 12 presents the results of a charge self-consistent KKR-CPA computation in $La_{1.7}Sr_{0.3}CuO_4$ for the ideal body-centered tetragonal lattice assuming

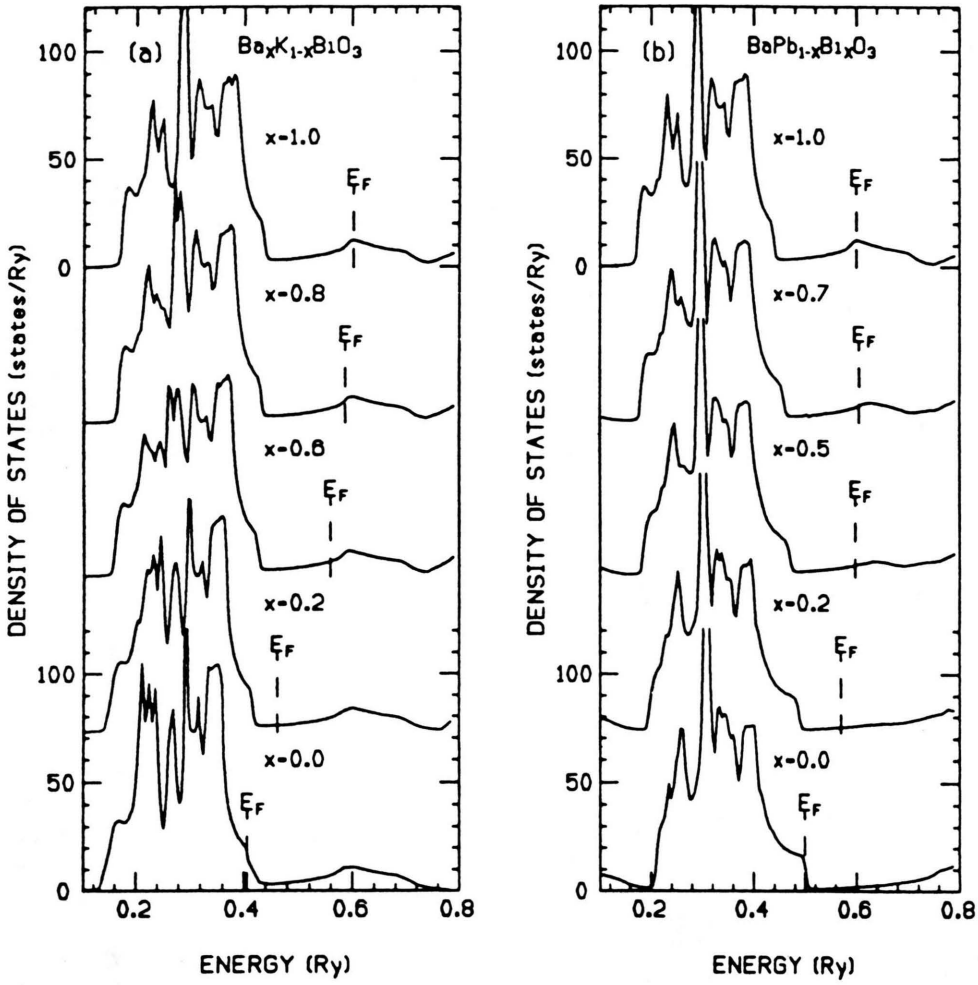

Fig. 10. Charge self-consistent KKR-CPA total densities of states in $Ba_xK_{1-x}BiO_3$ and $BaPb_{1-x}Bi_xO_3$. Fermi energies (E_F) are as marked (after [11]).

random occupation of the La-sites by La and Sr atoms, together with a corresponding self-consistent KKR calculation of the parent compound La_2CuO_4 [7]. The total density of states in La_2CuO_4 and $La_{1.7}Sr_{0.3}CuO_4$ is compared in Fig. 12, with Fig. 13 giving a more detailed comparison in the region of the E_F. Aside from an overall smoothing of the density of states, the main effect is the lowering of the E_F on substituting Sr for La; in particular, the shape of the density-of-states curve near E_F, Fig. 13, is hardly affected upon Sr-substitution. The component densities of states associated with the La- and Sr-sites in the alloy (not shown) are found to be rather similar. These *ab initio* results support the rigid band picture [45] of the electronic structure of $La_{2-x}Sr_xCuO_4$, based on band theory computations on La_2CuO_4, invoked commonly in the literature. (Note, however, that the physical compound La_2CuO_4 is insulating, not metallic as predicted by the band theory.) From the data of Fig. 13, we estimate that the E_F will in fact lie in the van Hove singularity in the density of states for approximately 20% Sr content (i.e. $x=0.20$) where the highest superconducting transition temperatures are experimentally observed.

III. Electron and Electron–Positron Momentum Densities in Alloys

a) Formalism

The electron momentum density $\varrho(\boldsymbol{p})$ is related to the $(\boldsymbol{p}, \boldsymbol{p})$ matrix element of the one-electron Green's

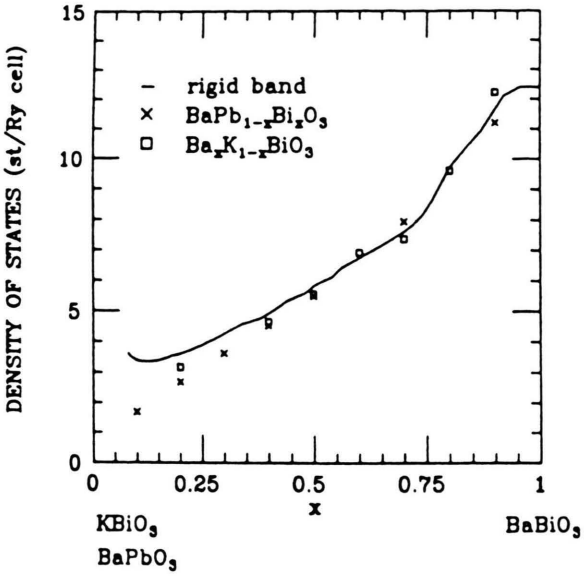

Fig. 11. Total density of states at the Fermi energy for the $BaBiO_3$-based rigid-band model, and the KKR-CPA results in $Ba_xK_{1-x}BiO_3$ and $BaPb_{1-x}Bi_xO_3$ (after [11]).

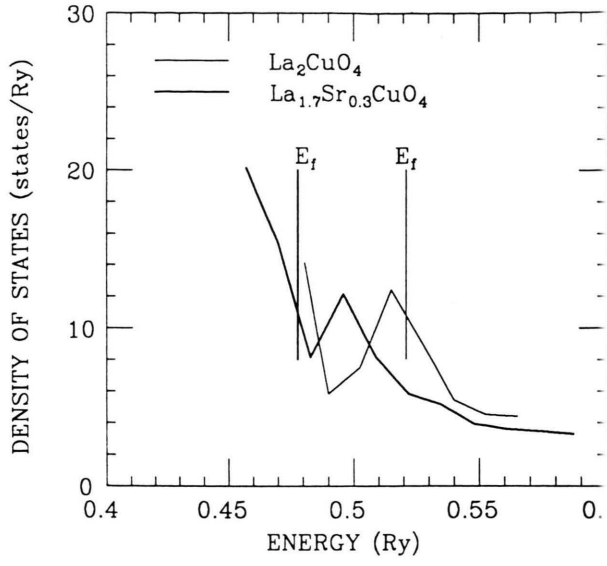

Fig. 13. The density of states near the Fermi energy (E_F) in La_2CuO_4 and $La_{1.7}Sr_{0.3}CuO_4$ (after [7]).

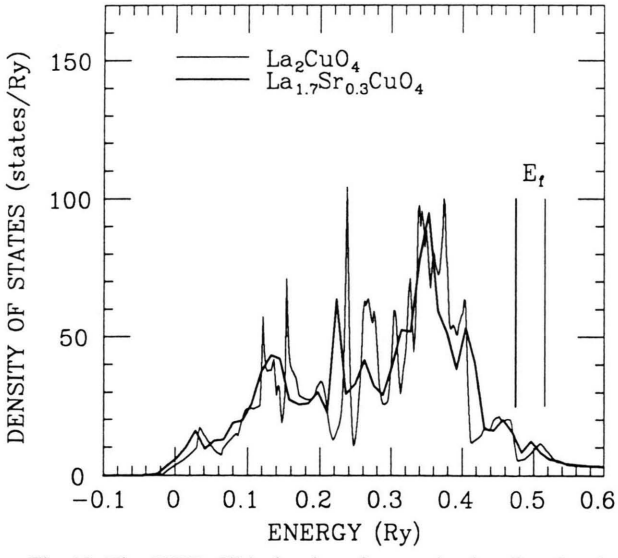

Fig. 12. The KKR-CPA density of states in the disordered $La_{1.7}Sr_{0.3}CuO_4$ is compared with the corresponding KKR results for La_2CuO_4 (after [7]).

function, in terms of which $\varrho(\boldsymbol{p})$ is expressed as [2, 21]

$$\varrho(\boldsymbol{p}) = -\frac{1}{\pi}\int_{-\infty}^{E_F} \mathrm{d}E\ \mathrm{Im}\langle G(\boldsymbol{p},\boldsymbol{p};E)\rangle\,. \tag{5}$$

Equation (5) is a convenient starting point for the calculation of the average momentum density in alloys, because $\langle G\rangle$ can be calculated within the framework of the CPA or the ATA theory.

The average electron-positron momentum density $\varrho_{2\gamma}(\boldsymbol{p})$ relevant for the angular correlation of (two-photon) annihilation radiation in a disordered alloy can similarly be expressed in terms of the electron and positron Green's functions as [2, 21]

$$\varrho_{2\gamma}(\boldsymbol{p}) = \frac{1}{\pi^2}\int \mathrm{d}\boldsymbol{r}\int \mathrm{d}\boldsymbol{r}'\exp[-i\boldsymbol{p}\cdot(\boldsymbol{r}-\boldsymbol{r}')] \cdot \int \mathrm{d}E\, f(E)\int \mathrm{d}E_+\, f_+(E_+) \cdot \langle \mathrm{Im}\, G(\boldsymbol{r},\boldsymbol{r}';E)\,\mathrm{Im}\, G_+(\boldsymbol{r},\boldsymbol{r}';E_+)\rangle\,, \tag{6}$$

where + refers to the positron quantities and $f(E)$ is the Fermi-Dirac distribution function. In the spirit of the independent-particle model (IPM), it is reasonable to decouple the average of $\langle \mathrm{Im}\, G\,\mathrm{Im}\, G_+\rangle$ as [46]

$$\langle \mathrm{Im}\, G\,\mathrm{Im}\, G_+\rangle \rightarrow \mathrm{Im}\langle G\rangle\,\mathrm{Im}\langle G_+\rangle\,. \tag{7}$$

Form (7) is expected to be a good approximation in transition and noble metal alloys [47]. Use of the convolution theorem on the right-hand side of (6) then yields

$$\varrho_{2\gamma}(\boldsymbol{p}) = \frac{1}{\pi^2}\sum_{k^+}\int \mathrm{d}E\, f(E)\int \mathrm{d}E_+\, f_+(E_+) \cdot \sum_{nn'}\langle \mathrm{Im}\, G(\boldsymbol{p}-\boldsymbol{k}_+-\boldsymbol{K}_n,\boldsymbol{p}-\boldsymbol{k}_+-\boldsymbol{K}_{n'};E)\rangle \cdot \langle \mathrm{Im}\, G_+(\boldsymbol{k}_+ + \boldsymbol{K}_n,\boldsymbol{k}_+ + \boldsymbol{K}_{n'};E_+)\rangle\,. \tag{8}$$

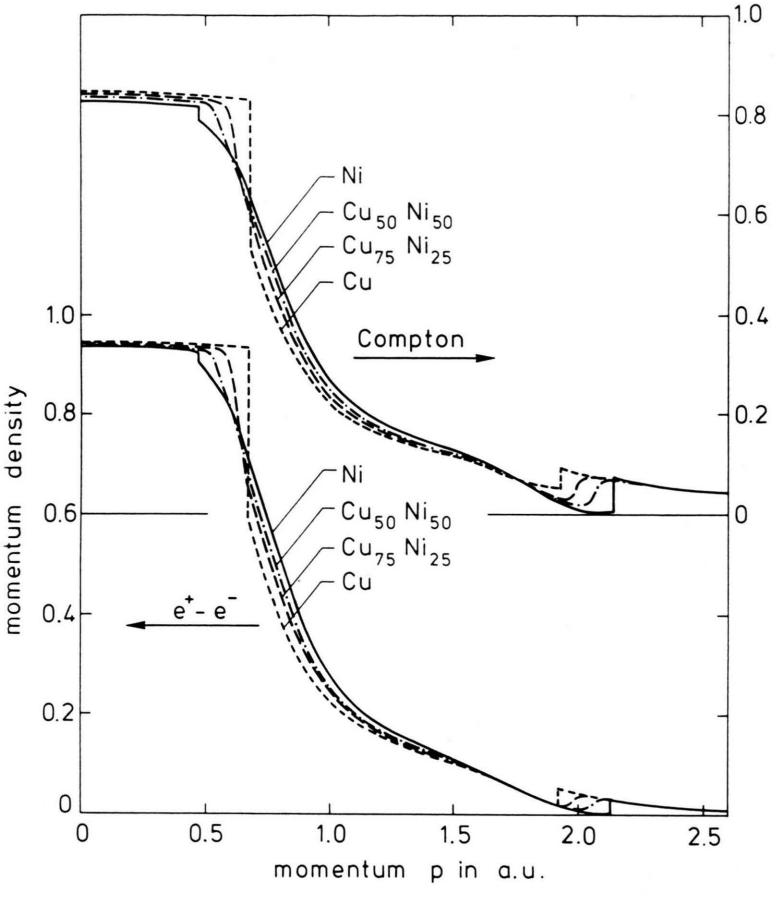

Fig. 14. Electron momentum density $\varrho(\boldsymbol{p})$ (upper set of curves) and electron-positron momentum density $\varrho_{2\gamma}(\boldsymbol{p})$ (lower set of curves) in Cu, $Cu_{75}Ni_{25}$, $Cu_{50}Ni_{50}$, and Ni along the [110] direction (after [46]).

It is noteworthy that the evaluation of $\varrho(\boldsymbol{p})$ requires only the diagonal elements $\mathrm{Im}\langle G(\boldsymbol{p}, \boldsymbol{p})\rangle$, whereas in order to compute $\varrho_{2\gamma}(\boldsymbol{p})$ a knowledge of the general elements $\mathrm{Im}\langle G(\boldsymbol{p}, \boldsymbol{q})\rangle$ and $\mathrm{Im}\langle G_+(\boldsymbol{p}, \boldsymbol{q})\rangle$ is necessary (see [46–48] for details of these and other aspects of the relevant formalism).

Effects of electron-positron correlations, neglected in writing (6) and (8), should be included in a proper theory of $\varrho_{2\gamma}(\boldsymbol{p})$. The semi-empirical "momentum" as well as "energy" and angular-momentum dependent enhancement schemes of the sort that have been invoked by various authors in perfect metals should be adapted to the case of alloys [49].

The experiments usually do not measure the three-dimensional functions $\varrho(\boldsymbol{p})$ and $\varrho_{2\gamma}(\boldsymbol{p})$ but only their one or two-dimensional integrals in momentum space. The Compton experiment is related to the two-dimensional integral [22, 23]

$$J(p_z) = \iint \mathrm{d}p_z\, \mathrm{d}p_y\, \varrho(\boldsymbol{p})\,, \tag{9}$$

where $\varrho(\boldsymbol{p})$ is the electron momentum density. Similarly, the older 1 D-ACAR experiment measures a two-dimensional integral of $\varrho_{2\gamma}(\boldsymbol{p})$, but the 2 D-ACAR experiment, on the other hand, resolves *two* momentum components and measures the one-dimensional integral $\varrho_{2\gamma}(\boldsymbol{p})$ along a specific line in momentum space, i.e. [19–21]

$$N_{2\gamma}(p_x, p_y) = \int_{-\infty}^{+\infty} \mathrm{d}p_z\, \varrho_{2\gamma}(p_x, p_y, p_z)\,, \tag{10}$$

where we have assumed that the axis of the positron camera is aligned along the z-axis.

b) Illustrative Examples

Figures 14 and 15 provide illustrative $\varrho(\boldsymbol{p})$ and $\varrho_{2\gamma}(\boldsymbol{p})$ results in CuNi solid solutions [46]. The upper set of curves in Fig. 14 shows that some of the changes in $\varrho(\boldsymbol{p})$, as we go from Ni to Cu, are: (i) the break at approximately 0.5 a.u. in Ni in the first Brillouin zone

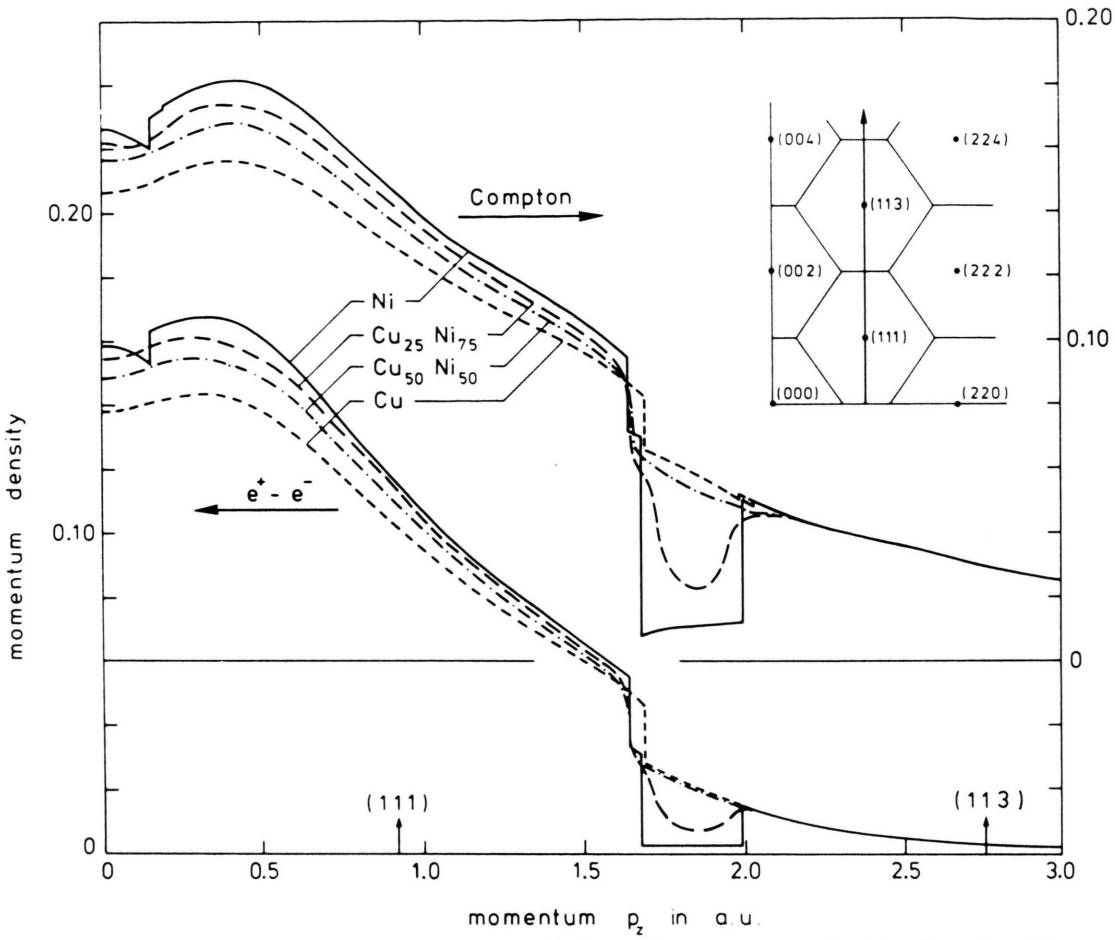

Fig. 15. Same as the caption of Fig. 14, except that this figure gives momentum densities along the off-the-zone-center direction joining the [111] and [113] reciprocal-lattice points (see inset) (after [46]).

(BZ) moves to higher momenta on alloying, and the size of the break increases; this results from an increase in the [110] Fermi Surface (FS) radius k_{110} and of the s-p character of the associated states with increasing Cu concentration. (ii) The [110] FS radius also yields "Umklapp" breaks in $\varrho(\boldsymbol{p})$ around $p = 2$ a.u.; these breaks move to correspondingly lower momenta with increasing k_{110}. (iii) In the alloys the breaks are not sharp but are rounded owing to disorder scattering of electrons. The preceding changes are seen to persist qualitatively in the lower set of curves for $\varrho_{2\gamma}(\boldsymbol{p})$. However, the $\varrho_{2\gamma}(\boldsymbol{p})$ curves decrease more rapidly with p compared to $\varrho(\boldsymbol{p})$ and thus appear to be more peaked in the first BZ. This difference between $\varrho(\boldsymbol{p})$ and $\varrho_{2\gamma}(\boldsymbol{p})$, which occurs more generally, is a consequence of the nuclear repulsion of the positron.

Figure 15 considers the momentum density along an off-the-zone-center direction. The particular direction shown is interesting because a dip is seen around $p_z = 1.8$ a.u. in Ni and $Cu_{25}Ni_{75}$ but not in Cu or $Cu_{50}Ni_{50}$; this dip arises from the presence of d-hole pockets in the Ni-rich alloys. It turns out that, owing to momentum and angular momentum selection rules, the disappearance/appearance of d-holes does not cause a dramatic change in the momentum density in the first BZ, but larger effects occur along the off-center direction at higher momenta in Figure 15. By comparing the upper and lower set of curves, we further note that this dip continues to be seen clearly even when the positron spatial distribution effects are included, although the size of the dip is reduced.

Figure 16 considers the Compton profile $J(q)$ (q is the p_z of (9) after spherical averaging) in polycrystalline

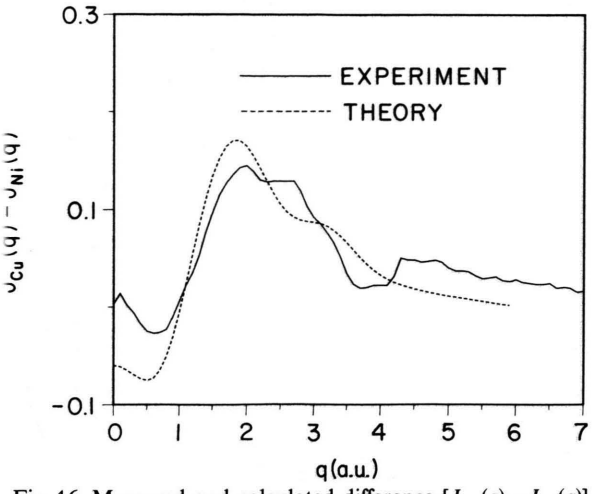

Fig. 16. Measured and calculated difference $[J_{Cu}(q) - J_{Ni}(q)]$ between the Cu and Ni Compton profiles (after [50]).

CuNi alloys [50]. The agreement for $J_{Cu} - J_{Ni}$ between theory and experiment is seen to be good, despite the fact that $|J_{Cu} - J_{Ni}|$ is at most a few percent of the value of $J_{Cu}(q)$. Both curves in the figure show a minimum at $q \approx 0.6$ a.u. This feature is associated with the condition $\varrho_{Cu}(p) = \varrho_{Ni}(p)$, which indeed occurs around a p value of 0.6 a.u. in CuNi alloys close to the FS break in Cu in the first BZ (see e.g., Fig. 14); the maximum at $q \approx 2$ a.u. possesses the same physical origin and reflects the position of the FS break in the fourth BZ. The broad dip around $q = 4$ a.u. in the solid curve is an artifact of the experiments and is not physically important; it has to do with the K-electron contribution, which, owing to experimental conditions, is included in the spectra in the range of 3.3–4.3 a.u. only in $J_{Ni}(q)$, but not in $J_{Cu}(q)$. Ref. [50] further compares KKR-CPA calculations with Compton measurements on CuNi alloys and finds a good overall agreement for the entire range of compositions. These results suggest that it may be possible to extract useful information concerning FS geometry from high-resolution Compton experiments on alloys, especially if single crystals are used.

Turning to **Cu**Ge and **Cu**Pd systems, Figs. 17 and 18 show that very substantial changes occur in $\varrho(\boldsymbol{p})$ as Cu is alloyed with Ge or Pd. $\varrho(\boldsymbol{p})$ in Cu is flat and featureless in the first BZ, but in **Cu**Ge it develops a pronounced peak and in **Cu**Pd a dip at $\boldsymbol{p} = 0$ [38, 40]. These effects contrast sharply with the case of **Cu**Ni alloys discussed in Fig. 14 where the momentum density remains quite flat in the first BZ. Owing to momentum and angular momentum selection rules,

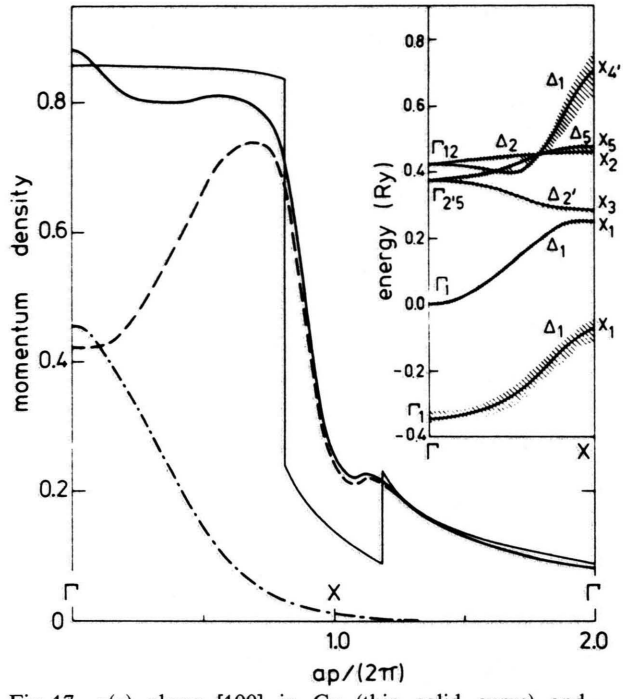

Fig. 17. $\varrho(\boldsymbol{p})$ along [100] in Cu (thin solid curve) and $Cu_{90}Ge_{10}$ (heavy solid curve). Contributions to $\varrho(\boldsymbol{p})$ in the alloy for $E \geq 0$ (dashed) and $E < 0$ (chain curve) are shown. The inset gives the complex band structure of $Cu_{90}Ge_{10}$ (after [38]).

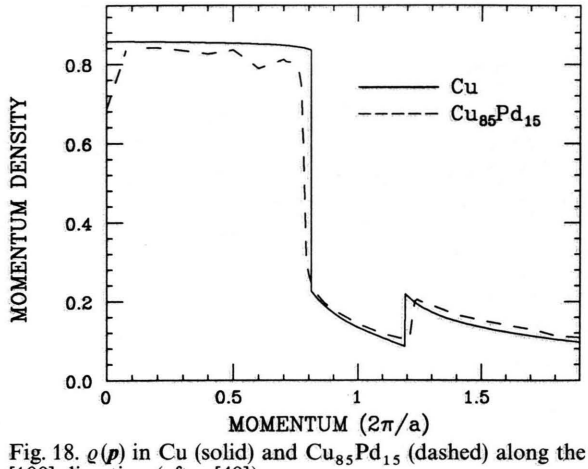

Fig. 18. $\varrho(\boldsymbol{p})$ in Cu (solid) and $Cu_{85}Pd_{15}$ (dashed) along the [100] direction (after [40]).

$\varrho(\boldsymbol{p})$ at $\boldsymbol{p}=0$ arises from states around the valence band edge; in particular, the d-bands do not contribute to $\varrho(\boldsymbol{p})$ at $\boldsymbol{p}=0$. The electron states at the valence band edge, which lie some 10 eV below the Fermi energy E_F, are difficult to access experimentally; in photoemission, for example, these states possess

rather small intensities and are masked by background and secondary emissions. **Cu**Ge and **Cu**Pd thus provide striking examples where alloying effects deep in the spectrum produce clear signatures in $\varrho(\boldsymbol{p})$.

The question of the extent to which the 2D-ACAR spectra in **Cu**Ge and **Cu**Pd reflect the behavior of $\varrho(\boldsymbol{p})$ near $\boldsymbol{p}=0$ is considered in [38] and [40]. Ref. [38] in particular shows that a bump near $\boldsymbol{p}=0$ appears in the theoretical as well as the experimental 2D-ACAR derivative spectra in **Cu**Ge. This bump is not present in Cu, and arises from the aforementioned peak in $\varrho(\boldsymbol{p})$ near $\boldsymbol{p}=0$ and constitutes a signature of the Ge-derived impurity band of s-p character (the lower Δ_1 band in the inset in Fig. 17); the agreement between theory and experiment in this regard offers evidence for the existence of this Ge-derived band in the alloy and a confirmation of these KKR-CPA predictions.

In this vein, [40] compares cuts through the 2D-ACAR measurements in **Cu**Pd alloys and shows that the experimental curves near $\boldsymbol{p}=0$ become distinctly flatter in the alloy. This feature is reproduced in the theoretical KKR-CPA computations (not shown), and arises substantially from the dip in $\varrho(\boldsymbol{p})$ near $\boldsymbol{p}=0$ discussed in connection with Fig. 18 above. These results, like those on **Cu**Ge, indicate that 2D-ACAR experiments can yield information concerning rather subtle features of the electronic spectrum, if they are used in parallel with corresponding theoretical work.

IV. Conclusions

We have discussed the basic concepts in the modern band theory of alloys that is based on the application of the CPA to treat disorder effects within the framework of the muffin-tin Hamiltonian. The nature of the spectral density function in the alloy, and its representation in terms of complex energy bands and a Fermi surface possessing finite disorder-induced smearing is stressed. During the last year or so, the KKR-CPA methodology has been generalized to provide a powerful charge and spin self-consistent parameter-free treatment of the electronic structure and properties of complicated materials possessing many atoms in the unit cell. These developments will permit a first-principles discussion of the effects of various substitutions and of oxygen-vacancy disorder in the disordered phases of the high-T_c superconductors and other complex materials.

The nature of the electron momentum density, $\varrho(\boldsymbol{p})$, relevant for the Compton scattering experiment, and of the electron-positron momentum density, $\varrho_{2\gamma}(\boldsymbol{p})$, involved in a positron annihilation (ACAR) measurement is clarified with reference to various suitable examples of binary alloys. To date, no computation of momentum density in a disordered alloy system with many atoms per unit cell has appeared in the literature, although the necessary methodology involves a straightforward generalization of the existing KKR-CPA machinery to obtain momentum densities. A significant effort has, however, been devoted to exploring the band theory predictions of the momentum density in the *ordered* high-T_c superconductors in the last few years [51].

We conclude by making a point concerning the investigation of Fermiology of high-T_c superconductors and other complex materials via Compton scattering and positron annihilation 2D-ACAR experiments. Note that the positron will in general sample the unit cell of the material in a non-uniform manner, as is abundantly clear from the recent experience with the high-T_c superconductors [51, 52]. Therefore, the 2D-ACAR spectrum will sample various electronic bands and the associated Fermi surfaces also in a non-uniform manner, e.g. in $YBa_2Cu_3O_7$ the positron spectrum preferentially responds to the electron chain bands and the related Fermi surfaces. The Compton scattering experiment, on the other hand, will sample the unit cell essentially uniformly. It is clear then that the combined use of these two spectroscopies will be most worthwhile in delineating the Fermiology of complex materials, especially with recent improvements in the momentum resolution of the Compton technique.

Acknowledgements

This project is supported by the US Department of Energy contract W-31-109-ENG-38, including a subcontract to Northeastern University, and benefited from the allocation of supercomputer time on the ER-Cray at NERSC, and the San Diego and Pittsburgh Supercomputer Centers. We also acknowledge partial support from the Research and Scholarship Development Fund (RSDF) of Northeastern University, and a travel grant from NATO and the US/Finland program of the NSF.

[1] A. Bansil, in: Electronic Band Structure and its Applications, Lecture Note Series, Vol. 283 (M. Yussouff, ed.). Springer-Verlag, Heidelberg 1987, p. 273.

[2] A. Bansil, in: Positron Annihilation (P. G. Coleman, S. G. Sharma, and L. M. Diana, eds.), North-Holland Publ., Amsterdam 1982, p. 291.

[3] H. Ehrenreich and L. M. SChwartz, in: Solid State Physics, Vol. 31 (H. Ehrenreich, F. Seitz, and D. Turnbull, eds.), Academic Press, New York 1976.
[4] G. M. Stocks and H. Winter, in: Electronic Structure of Complex Systems (P. Phariseau and W. Temmerman, eds.), Plenum Press, New York 1984.
[5] J. S. Faulkner, in: Progress in Materials Sciences (T. Massalski, ed.), Pergamon Press, New York 1982, Vol. 27.
[6] L. Schwartz, in: Excitations in Disordered Systems (M. F. Thorpe, ed), Plenum Press, New York 1982.
[7] A. Bansil, S. Kaprzyk, and J. Toboła, in: Applications of Multiple Scattering Theory to Materials Science (W. H. Butler, A. Gonis, and R. Weaver, eds.), Mat. Res. Society 1992. This volume also contains a recent discussion of various applications to alloys.
[8] See J. Kudrnovsky, V. Drchal, M. Sob, N. E. Christensen, and O. K. Anderson, Phys. Rev. B **40,** 10029 (1989), and references therein, for work applying CPA within the LMTO framework to disordered alloys.
[9] The analytic properties of the CPA theory are discussed by a number of authors, see, L. Schwartz and A. Bansil, Phys. Rev. B **21,** 4322 (1980). – T. Kaplan, P. L. Leath, L. J. Gray, and H. W. Diehl, Phys. Rev. B **21,** 4230 (1980). – R. Mills, L. J. Gray, and T. Kaplan, Phys. Rev. B **27,** 3252 (1983). – F. Ducastle, J. Phys. C **7,** 1785 (1974). – An-Ban Chen, Phys. Rev. B **7,** 2230 (1973).
[10] S. Kaprzyk and A. Bansil, Phys. Rev. B **42,** 7358 (1990).
[11] A. Bansil and S. Kaprzyk, Phys. Rev. B **43,** 10335 (1991).
[12] For a general discussion of complex-energy methods applied to the muffin-tin systems, see, B. Drittler, M. Weinert, R. Zeller, and P. Dederichs, Phys. Rev. B **39,** 930 (1989), and references therein.
[13] For a discussion of relativistic effects, see, e.g., P. Weinberger, in: Actinides in Perspective (Edelstein, M. Norman, ed.), Pergamon Press, Oxford 1982. – E. Arola, Acta Polytechnica Scandinavica, Appl. Phys. Series 174, Helsinki 1991, and references therein.
[14] For magnetic effects in alloys, see, e.g., J. B. Staunton, B. L. Gyorffy, D. D. Johnson, F. J. Pinski, and G. M. Stocks, in: Alloy Phase Stability (G. M. Stocks, and A. Gonis, eds.), Kluwer, Dordrecht 1987.
[15] See [16] and [17] for reviews of photoemission studies of alloys.
[16] A. Bansil and M. Pessa, Physica Scripta T **4,** 52 (1983).
[17] P. J. Durham, in: The Electronic Structure of Complex Systems (P. Phariseau and W. M. Temmerman, eds.), Plenum Press, New York 1984.
[18] See [2] and [19–25] for reviews of momentum densities in alloys.
[19] S. Berko, in: Positron Solid State Physics (W. Brandt and A. Dupasquier, eds.), North-Holland Publ., Amsterdam 1983.
[20] R. N. West, in: Positron Annihilation (P. C. Jain, R. M. Singru, and K. P. Gopinathan, eds,), World Scientific, Singapore 1985, p. 11.
[21] P. E. Mijnarends, phys. stat. sol. (a) **102,** 31 (1987).
[22] See, for example, Compton Scattering (B. G. Williams, ed.), McGraw-Hill Book Co., New York 1977; for a collection of articles on the subject.
[23] M. J. Cooper, Rep. Prog. Phys. **48,** 415 (1985), also this conference.
[24] S. Berko, in: Momentum Distributions (R. N. Silver and P. E. Sokol, eds.), Plenum Press, New York 1989, p. 273.
[25] P. E. Mijnarends, in: Positrons in Solids, Course LXXXIII, International School of Physics "Enrico Fermi", North-Holland Publ., Amsterdam 1982.
[26] A. Bansil, L. Schwartz, and H. Ehrenreich, Phys. Rev. B **12,** 2893 (1975). – A. Bansil, Phys. Rev. B **20,** 4035 (1979). – A. Bansil, Phys. Rev. Letters **41,** 1670 (1978).
[27] A. Bansil, H. Ehrenreich, L. Schwartz, and R. E. Watson, Phys. Rev. B **9,** 455 (1974).
[28] H. Asonen, M. Lindroos, M. Pessa, R. Prasad, R. S. Rao, and A. Bansil, Phys. Rev. B **25,** 7075 (1982). – M. Pessa, H. Asonen, R. S. Rao, R. Prasad, and A. Bansil, Phys. Rev. Letters **47,** 1223 (1981).
[29] R. Prasad and A. Bansil, Phys. Rev. Letters **48,** 113 (1982).
[30] E. Arola, R. S. Rao, A. Salokatve, and A. Bansil, Phys. Rev. B **41,** 7361 (1990). – E. Arola, C. J. Barnes, R. S. Rao, and A. Bansil, Phys. Rev. B **42,** 8820 (1990).
[31] A. Bansil, R. S. Rao, R. Prasad, H. Asonen, and M. Pessa, J. Phys. F **14,** 273 (1984).
[32] E. Arola, C. J. Barnes, R. S. Rao, A. Bansil, and M. Pessa, Surface Sci. **249,** 281 (1991).
[33] For dHvA studies of alloys, see, P. T. Coleridge, in: Electrons at the Fermi Surface (M. Springford, ed.), Cambridge Univ. Press, Cambridge 1980.
[34] R. Prasad, S. C. Papadopoulos, and A. Bansil, Phys. Rev. B **23,** 2607 (1981).
[35] M. Haghgooie, S. Berko, and U. Mizutani, in: Positron Annihilation (R. R. Hasiguti and K. Fujiwara, eds.), Japan Inst. of Metals, Sendai 1979.
[36] J. G. McLarnon and D. L. Williams, J. Phys. Soc. Japan **43,** 1244 (1977). – To. Suzuki, M. Hasegawa, and M. Hirabayashi, Appl. Phys. **5,** 269 (1974).
[37] P. T. Coleridge and I. M. Templeton, Can. J. Phys. **49,** 2449 (1971).
[38] P. E. Mijnarends, L. P. L. M. Rabou, K. E. H. M. Hanssen, and A. Bansil, Phys. Rev. Letters **59,** 720 (1987).
[39] A. Bansil, R. Prasad, S. Bessendorf, L. Schwartz, W. J. Venema, B. Feenstra, F. Blom, and R. Griessen, Sol. State Commun. **32,** 1115 (1979).
[40] L. C. Smedskjaer, R. Benedek, R. W. Siegel, D. G. Legnini, M. Stahulak, and A. Bansil, Phys. Rev. Letters **59,** 2479 (1987).
[41] B. L. Gyorffy and G. M. Stocks, Phys. Rev. Letters **50,** 374 (1983).
[42] R. S. Rao, A. Bansil, H. Asonen, and M. Pessa, Phys. Rev. B **29,** 1713 (1984).
[43] L. F. Mattheiss and D. R. Hamann, Phys. Rev. Letters **60,** 2681 (1988).
[44] D. A. Papaconstantopoulos, A. Pasturel, J. P. Julien, and F. Cyrot-Lackmann, Phys. Rev. B **40,** 8844 (1989).
[45] For recent reviews of high-T_c's, see, K. C. Hass, Solid State Physics **42,** 213 (1989). – W. E. Pickett, Rev. Mod. Phys. **61,** 433 (1989).
[46] A. Bansil and P. E. Mijnarends, Phys. Rev. B **30,** 628 (1984).
[47] Z. Szotek, B. L. Gyorffy, G. M. Stocks, and W. M. Temmerman, J. Phys. F **14,** 2571 (1984).
[48] A. Bansil, R. S. Rao, P. E. Mijnarends, and L. Schwartz, Phys. Rev. B **23,** 3608 (1981).
[49] For methods of including electron-positron correlations, see E. Boronski and R. M. Nieminen, Phys. Rev. B **34,** 3820 (1985). – T. Jarlborg and A. K. Singh, Phys. Rev. B **36,** 4660 (1987). – J. Arponen and E. Pajanne, J. Phys. F **9,** 2359 (1979). – H. Sormann and M. Sob, Phys. Rev. B **41,** 10529 (1990). – P. E. Mijnarends and R. M. Singru, Phys. Rev. B **19,** 6038 (1979).
[50] R. Benedek, R. Prasad, S. Manninen, B. K. Sharma, A. Bansil, and P. E. Mijnarends, Phys. Rev. B **32,** 7650 (1985).
[51] See A. Bansil, J. Phys. Chem. Solids **52,** 1493 (1991); also L. C. Smedskjaer and A. Bansil, Z. Naturforsch. **48a,** 398 (1993).
[52] D. Singh, W. E. Pickett, R. E. Cohen, H. Krakauer, and S. Berko, Phys. Rev. B **39,** 9667 (1989).